Segmentation of Coronary Arteries from X-ray Angiographic Images Using a Combination of K-Nearest Neighbor Clustering and Morphological Reconstruction Techniques

K. Mardani^{a}, K. Maghooli^{b,*} and F. Farokhi^{a}

^{a}Department of Biomedical Engineering, Central Tehran Branch, Islamic Azad University, Tehran, Iran
^{b}Department of Biomedical Engineering, Science and Research Branch, Islamic Azad University, Tehran, Iran

Coronary angiography is an X-ray procedure used to examine the arteries of the heart. It provides information about the presence and severity of heart disease and helps doctors assess how well the heart is functioning. This study introduces a new technique for segmenting the coronary arteries in X-ray angiographic images using K-nearest neighbors clustering. The method involves separating thick and thin veins into distinct spaces and then merging them together. To eliminate noise and extract the vessel tree accurately, the algorithm employs morphological techniques like reconstruction, skeletonization, pruning, and dilation, as well as filters such as mean and convolution filters. The resulting segmented vessel tree contains several newly identified thin vessels that have low light intensity in the original image. The algorithm's efficacy is demonstrated by comparing the results with ground truth images. The evaluation criteria, including an accuracy of 0.9747, specificity of 0.9784, and sensitivity of 0.9049, indicate favorable performance compared to other methods. Additionally, the performance of this method is assessed using multiple lesions and instances of vessel blockages.

topics: coronary vessel segmentation, X-ray angiography, K-nearest neighbor (KNN), pattern recognition

1. Introduction

Angiography is a medical imaging procedure that serves both diagnostic and therapeutic purposes by providing visual representations of the inside of blood vessels, arteries, and the heart. It involves the administration of a radioactive contrast substance into the bloodstream, followed by imaging using X-ray-based techniques like fluoroscopy. This enables health care professionals to obtain detailed images of the blood vessels and assess their condition. Angiography is employed to identify issues such as the narrowing and blockage of blood vessels, as well as other problems related to the circulatory system. The procedure typically involves administering sedation to the patient. The duration of the angiogram varies depending on the complexity of the examination and the duration of the treatment, ranging from 15 to 20 min or even several hours. Generally, the angiogram commences with the insertion of a needle into the femoral artery located in the groin area, which serves as an entry point to access the blood vessels. Once access to the arterial system is established, catheters (thin tubes) and wires are guided through the arteries to the desired location. A radioactive substance is then injected, and X-ray images are captured. This enables visualization of the blood flow within the vessels and identification of areas where vascular blockages exist. Based on the findings of the angiography, along with the patient's symptoms and the severity and characteristics of the blockage, the doctor determines the appropriate treatment approach. If a vascular blockage is detected, two common treatment methods performed during angiography are balloon angioplasty (placement of a balloon) and stent placement (insertion of a spring-like device) [1, 2]. Angioplasty is a procedure performed to clear a blockage in an artery. Using X-ray guidance, the doctor guides a specialized device, which consists of an inflatable balloon attached to a wire, through the blockage. Once positioned in the blocked area of the artery, the balloon is inflated to open up the artery and compress the blockage. Afterward, while the wire is kept in place within the treated area, the balloon is deflated and removed. To assess the

outcome, a dye is injected into the blood vessels. If the blood flow improves and the blockage is reduced to less than 30%, the treatment is considered successful. However, if the artery is still significantly narrowed, the next step may involve placing a stent. Stents are utilized to widen a narrowed artery. Typically, stents are permanently placed either after balloon angioplasty or when there is inadequate blood flow in a treated blood vessel. In the case of leg stents, they are constructed from a nickel-titanium alloy known as nitinol. These stents possess both durability and flexibility [3, 4].

Over the past two decades, numerous methods for segmenting blood vessels have been utilized, targeting various medical imaging techniques. Nevertheless, there is no single blood vessel segmentation method that can effectively handle all types of images. The reviews conducted by Kirbas and Quek [5] and Lesage et al. [6], as well as the thesis works by Läthén [7] and Drechsler [8], offer valuable insights into the blood vessel segmentation methods discussed in the existing literature. To summarize, various blood vessel segmentation methods can be categorized into vessel enhancement, thresholding, region growth, deformable models, and centerline tracking. Vessel enhancement is commonly employed as a preliminary step in many approaches to enhance the visibility of the vessel structure in the image, while other methods are predominantly utilized to segment these structures.

This article introduces an algorithm that addresses certain challenges related to vessel segmentation. Some of these issues can be resolved through density-based clustering [9]. The proposed method utilizes a straightforward algorithm centered on *K*-nearest neighbor (KNN) to accomplish vessel segmentation, correct gaps between vessels, and extract a complete vessel tree from the original image. The KNN algorithm is employed for vessel segmentation in two distinct spaces, distinguishing between narrow and wide vessels. By merging these results, it becomes possible to significantly reduce noise. Notably, the proposed method exhibits the capability to perform segmentation quickly and identify vessels with low light intensity. Furthermore, the proposed algorithm's applicability to various vascular diseases is explored.

2. Materials and methods

The heart is primarily supplied by two main arteries, i.e., the left coronary artery (LCA) and the right coronary artery (RCA). These arteries and their branches ensure the heart's blood supply. Specifically, LCA primarily provides blood to the left ventricle, while RCA supplies the right atrium and ventricle, the sinoatrial (SA) node, the inferior wall, the posterior interventricular septum, and the posteromedial papillary muscle in approximately 85% of cases [10].
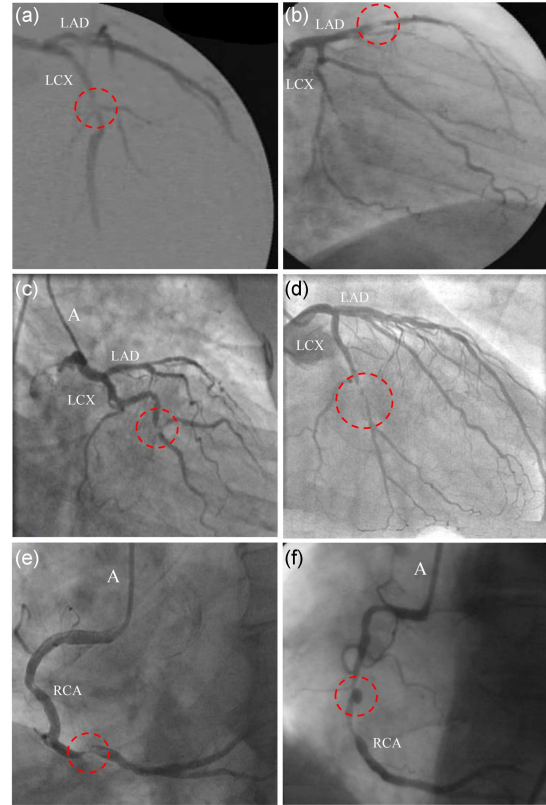

Fig. 1. A depiction of the vascular trees in the left and right sides of the heart, along with associated lesions: (a) left coronary artery (LCA) with a bifurcation lesion in LCX; (b) LCA with a lesion in LAD; (c) bifurcation in LCX along with the presentation of the catheter "A"; (d) LCA with a thrombus in LCX; (e) thrombus lesion on RCA; (f) mushroom-shaped lesion in RCA. Note: Fig. 1a and b comes from [11] and Fig. 1c–f from [10].

The left coronary artery usually runs for 1 to 25 mm as the left main artery before splitting into two branches, namely the anterior interventricular artery, also known as the left anterior descending (LAD) artery, and the left circumflex artery (LCX). If an artery arises from the left main artery between LAD and LCX, it is called the ramus intermedius. The ramus intermedius is found in 37% of the general population and is considered a normal variation (Fig. 1a–d, see also [10, 11]).

The right coronary artery (RCA) begins just above the right cusp of the aortic valve and follows a path down the groove between the right atrium and right ventricle, heading towards the center of the heart. Besides providing blood to the right ventricle (RV), RCA also contributes to the blood supply of approximately 25% to 35% of the left ventricle (LV). RCA has a curved, C-shaped appearance (Fig. 1e, f) [10].

The images utilized in this research were sourced from two databases. In the first database, which includes 130 angiography images, 32 were chosen randomly, and two of them exhibited some form

of vessel blockage. The images in this database measure 300×300 pixels and have limited contrast. They are accessible for use by the scientific community and made available by the Cardiology Department of the Mexican Social Security Institute, UMAE T1 León, under the R-2019-1001-078 license [12–18]. The second database comprises 4 angiography images, each with dimensions of 900×900 pixels. These images exhibit a higher level of contrast compared to those in the first database and were created using standard angiography techniques. From the chosen images in both databases, 17 left coronary artery (LCA) images and 19 right coronary artery (RCA) images were picked. In addition to depicting the vascular structure, 6 images also feature certain vascular diseases, which will be the focus of the proposed algorithm's performance assessment (Fig. 1). On these six sample images, the LAD, LCX, and RCA vessels are labeled. The disease's location is highlighted with red circles, and the catheter's external agent is marked with the letter "A". Images (a) and (c) in Fig. 1 depict the bifurcation lesion. Bifurcation lesions happen when atherosclerotic plaque affects the starting points of two distinct arteries. A bifurcation is described as the splitting of a primary, parent branch into two smaller daughter branches, each measuring at least 2.0 mm in diameter. Bifurcation lesions are frequent in cases of coronary artery disease (CAD), accounting for 15–18% of the lesions treated with percutaneous coronary intervention (PCI). Image (b) illustrates a lesion in LAD. Images (d) and (e) in Fig. 1 display thrombus blockages in LCX and RCA. A coronary artery thrombus can be described as a blockage or obstruction of blood flow within a blood vessel caused by a blood clot. Image (f) in Fig. 1 depicts a mushroom lesion. An ulcerated lesion is defined as a cavity in the vessel wall with a disruption of the intima and flow observed within the plaque cavity. The coronary artery ulceration is assessed visually using a well defined grading system. Grade 0 corresponds to no angiographic evidence of ulceration, grade 1 ulceration is present when the lesion contains a neck with contrast material dissecting under the plaque either proximally or distally, and grade 2 ulceration is present when there is distinct extravascular extravasation of a contrast material with the appearance of a mushroom [10].

By combining image subtraction with opening and closing operations, we obtain what is known as the top-hat and bottom-hat transformations. The top-hat transformation of a grayscale image f is defined as the difference between f and its corresponding opening, i.e.,

$$T_{hat}(f) = f - (f \circ b). \tag{1}$$

Similarly, the bottom-hat transformation of f is defined as the result of closing f subtracted from f, i.e.,

$$B_{hat}(f) = (f \bullet b) - f. \tag{2}$$

These transformations find a key application in eliminating objects from an image. This is achieved by employing a structuring element (b) in either the opening or closing operation, which does not match the objects intended for removal. The resulting difference operation produces an image where only the removed components persist. The top-hat transformation is utilized when dealing with light objects against a dark background, while the bottom-hat transformation is employed in the opposite scenario. Hence, the terms "white top-hat" and "black top-hat" are commonly used to refer to these respective transformations [19].

The KNN, or K-nearest neighbor, algorithm is a type of supervised machine learning algorithm used in both classification and predictive regression problems [20, 21]. Although it is commonly employed in the industry for predictive classification problems, KNN is considered a lazy learning algorithm because it lacks a specific learning step and utilizes all the data for learning during classification. Additionally, KNN is a parameter-free learning algorithm, as it does not make any assumptions about the original data. The KNN algorithm relies on "feature similarity" to make predictions for new data points. This means that it assigns a value to the new data point based on how closely it matches the points in the training set [22, 23]. The following steps will help in understanding how it works:

1. In order to implement any algorithm, we require a dataset. Therefore, the first step in KNN involves loading the training data along with the test data.

2. Next, we need to choose the value of K, which represents the number of closest data points to consider; K can be any integer.

3. Using one of the Euclidean methods, such as the Hamming distance or Manhattan distance, we calculate the distance between the test data and each entry in the training data. The most commonly used method for distance calculation is the Euclidean method.

4. Based on the calculated distance values, we sort them in ascending order.

5. The algorithm then selects the K rows with the smallest distances from the sorted array.

6. Finally, based on the most frequently occurring class among these selected rows, the algorithm assigns a class to the test point.

Figure 2 depicts the flowchart of the proposed algorithm. Initially, a complementary image is extracted from the input image (Fig. 3a, b) [11]. The input images follow two distinct paths within this method. On the left path, the top-hat transformation of the 3rd order is applied to them (Fig. 3c). Subsequently, the KNN algorithm carries out one-dimensional clustering independently using two functions, one in the horizontal direction and the other in the vertical direction. Since the images
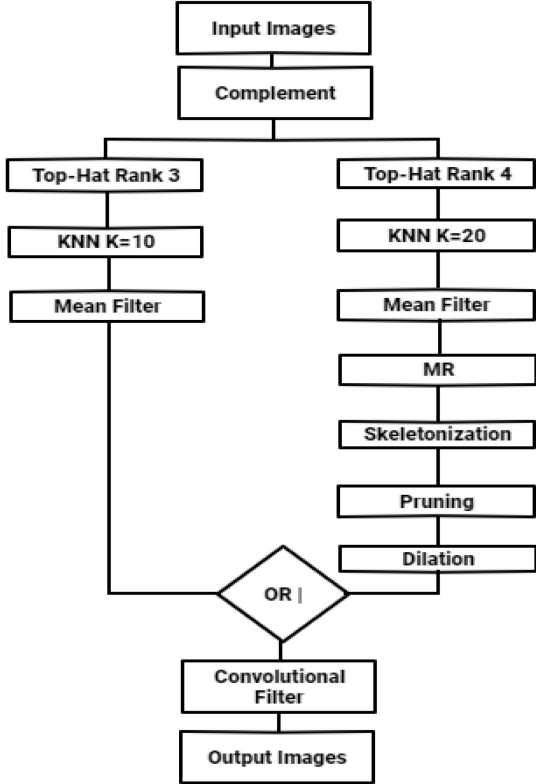
Fig. 2. Flowchart illustrating the proposed algorithm.

eliminate background noise (Fig. 3g). Morphological reconstruction is executed in a loop on the KNN image to progressively eliminate noise clusters in ascending order of their sizes. The process is iterative, reusing the modified image at each step. Essentially, MR diminishes the intensity of very bright points or clusters present on the vessels and noise, while enhancing the intensity of very dark points in the background. This uniformization process aims to bring consistency to both the background and foreground. Meanwhile, excessively bright or dark noises are typically eliminated. Among the resulting images obtained through MR, the most accurate image is selected to proceed to the next step in the left branch of the algorithm.

An operation known as closing by opening is carried out on the image to fill any potential gaps (Fig. 3h). Following this process, a skeletonization operation is performed (Fig. 3i). This action results in all veins, regardless of thickness, being transformed into narrow and uniform structures. Moreover, the remaining noise clusters in the image become significantly smaller. The skeletonization process not only preserves the structure of the vessel tree by converting it into thin vessels but also effectively eliminates the remaining noises to a significant degree.

The subsequent step after skeletonizing the vein tree involves pruning it (Fig. 3j). This process eliminates unnecessary branches that are attached to the vessels as a result of skeletonization, thereby bringing the vessel tree closer to its realistic form. A beneficial side effect of pruning is the reduction of residual noise in the image's background. In the continuation of the process, the pruned vein tree is expanded adequately to attain the thickness of thin veins (Fig. 3k). Subsequently, the thin veins are connected to the previously extracted thick veins, resulting in the complete vein tree pattern (Fig. 3l). After this step, the remaining noises appear as points of the same size, which can be eliminated using a mean convolutional filter (Fig. 3m). This filter possesses the ability to smoothen the borders of the vessels and make their brightness more consistent. The structure of this filter is as follows

$$F = \exp(-K) \begin{bmatrix} 1 & \cdots & 1 \\ \vdots & 1 & \vdots \\ 1 & \cdots & 1 \end{bmatrix}_{K \times K}. \qquad (3)$$

3. Results

In vessel segmentation, gold standard (GS) images are drawn manually by cardiologists, which are also called ground truth (GT) images. The evaluation of blood vessel segmentation is conducted using the gold standard, which involves the introduction of true positive (TP), true negative (TN), false positive (FP), and false negative (FN) parameters. Positive and negative refer

are of the uint8 type and the pixel intensity ranges from zero to 255, the neighborhood distance in the KNN algorithm is set to one. The K parameter, representing the number of neighbors, can be adjusted from one to any desired value to prevent the image from being overwhelmed by noise. In this particular method, values of 10 and 20 are chosen for K based on the thickness of thin and thick vessels, respectively (Fig. 3d, f). To enhance the accuracy of the algorithm, the main image is divided into smaller sub-images using a variable known as R. The KNN algorithm is initially applied to these sub-images, and subsequently, the sub-images are interconnected to form a vein tree pattern. The left branch focuses on segmenting the thicker veins, while the right branch is specifically designed for extracting narrow veins. In this branch, the images undergo contrast enhancement through the application of a top-hat transformation of order 4. Using a higher-order top-hat transformation aids in revealing thinner veins, albeit at the expense of increased noise. Within this branch, the KNN algorithm is executed with a minimum of 10 neighboring points ($K = 10$), as thin vessels are typically narrower and consist of fewer pixels. As a result, fewer and smaller noise clusters will arise. Following the application of KNN in both branches, a median filter is employed to eliminate the smaller clusters. Subsequently, the morphological reconstruction (MR) method [9] is utilized to
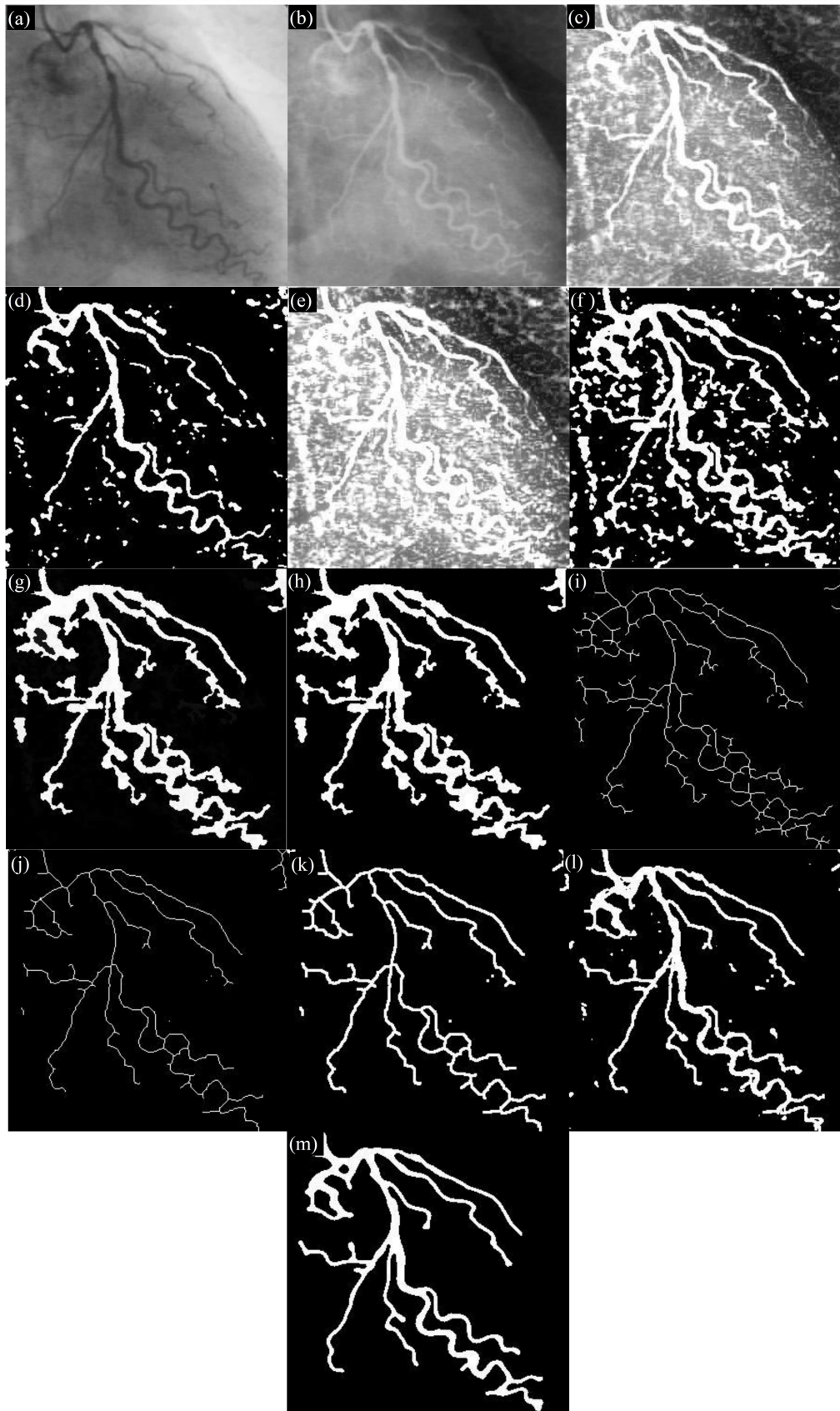
Fig. 3. The outputs of various components within the proposed algorithm: (a) original image; (b) complement; (c) top-hat rank 3; (d) KNN ($K = 10$) on image (c); (e) top-hat rank 4; (f) KNN ($K = 20$) on image (e); (g) MR; (h) closing by opening; (i) skeleton; (j) prune; (k) dilation; (l) fusion of images (d) and (k); (m) convolutional filter. Note: Fig. 3a comes from [11].
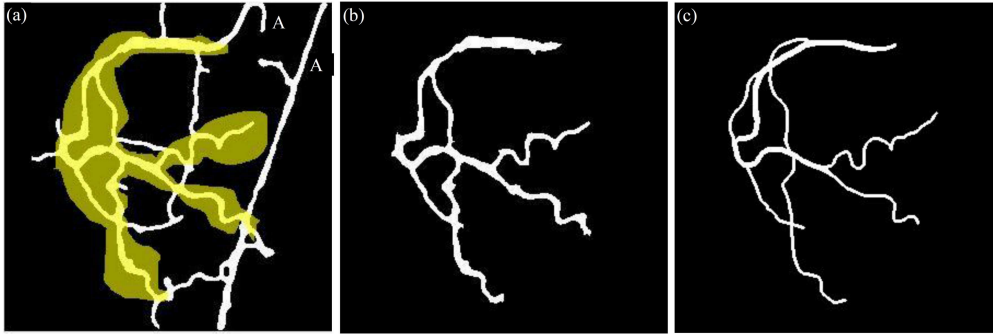
Fig. 4. Cropping the overlapping portion of the vessel tree in the algorithm's output image and the ground truth (GT) image to facilitate a more accurate numerical comparison of performance measures. Note: Fig. 4c comes from [11].

to pixels belonging to the arteries and the background of the image, respectively. In addition to these parameters, classification performance measures such as accuracy (ACC), sensitivity (SEN), and specificity (SPE) are widely utilized and considered among the most commonly used metrics in various segmentation approaches [24–27]. ACC and area under the curve (AUC) are commonly used as indicators of vessel segmentation performance. AUC represents the average of sensitivity (SEN) and specificity (SPE). SEN signifies the correct identification of vessels, while SPE represents non-vascular pixels that belong to the background or non-vessel regions. The Dice similarity coefficient (DSC) measures the similarity between the segmented vessel tree pattern and the ground truth (GT) pattern, disregarding correctly classified background pixels. A higher SEN value indicates better artery segmentation. The total number of pixels in the image, denoted as (n), is equal to TP + TN + FP + FN [28–30] (Table I).

To enhance the comparison of the algorithm's performance, we may encounter situations where, in addition to the catheter image recorded alongside the vessel tree, there could be overlapping images of other external devices like wires, pacemakers, and so on. This can alter the evaluation criteria and reduce the accuracy of vessel segmentation. Consequently, we utilize the Image Segmenter toolbox in the MATLAB software to crop and eliminate these items. Furthermore, the proposed method identifies narrower vessels on the GT (ground truth) image created by the cardiologist. Given that the evaluation relies on GT images and that other methods have similarly conducted their evaluations using these images, during the evaluation process and comparison of evaluation parameters, the newly identified vessels are temporarily excluded by the Image Segmenter tool.

This operation is illustrated in Fig. 4 (see also [11]). Panel (a) represents the output of the proposed algorithm, displaying a broader pattern of the vascular tree. Within it, you can observe the image of the tube created by the catheter and

TABLE I

Possible parameters and performance criteria of vessel segmentation algorithms.

Possible parameter		
GS (GT)		
	vein	non-vein
vein	TP	FP
non-vein	FN	TN
Performance measures		
Criteria	Description	
ACC	$\frac{TP+TN}{n}$	
SEN	$\frac{TP}{TP+FN}$	
SPE	$\frac{TN}{TN+FP}$	
AUC	$\frac{SEN+SPE}{2}$	
DSC	$\frac{2TP}{2TP+FP+FN}$	

wire (marked as A) and the newly discovered veins. Panel (b) displays what remains after removal, and panel (c) represents the ground truth (GT).

In this part of the section, in Fig. 5, we present the results obtained from the proposed algorithm. The images are sourced from the first database and include those from both the right and left coronary arteries of the heart. The rows labeled (a) display the original images, rows labeled (b) display the ground truth images, and rows labeled (c) display the segmented images (Fig. 5) (see also [11]).

The slender catheter tube, which connects to the entrance of the primary vessel in the angiographic images, is also visible in the segmented images, connected to the vessel tree. Upon comparing the segmented images with the original and ground truth (GT) images, one can observe a number of narrow vessels detected by the algorithm. Some of these newly identified vessels are marked with red rectangles. The segmentation of folds in the included images is well-executed, and in some cases, it appears to be more complete than in the ground truth images (Fig. 5).
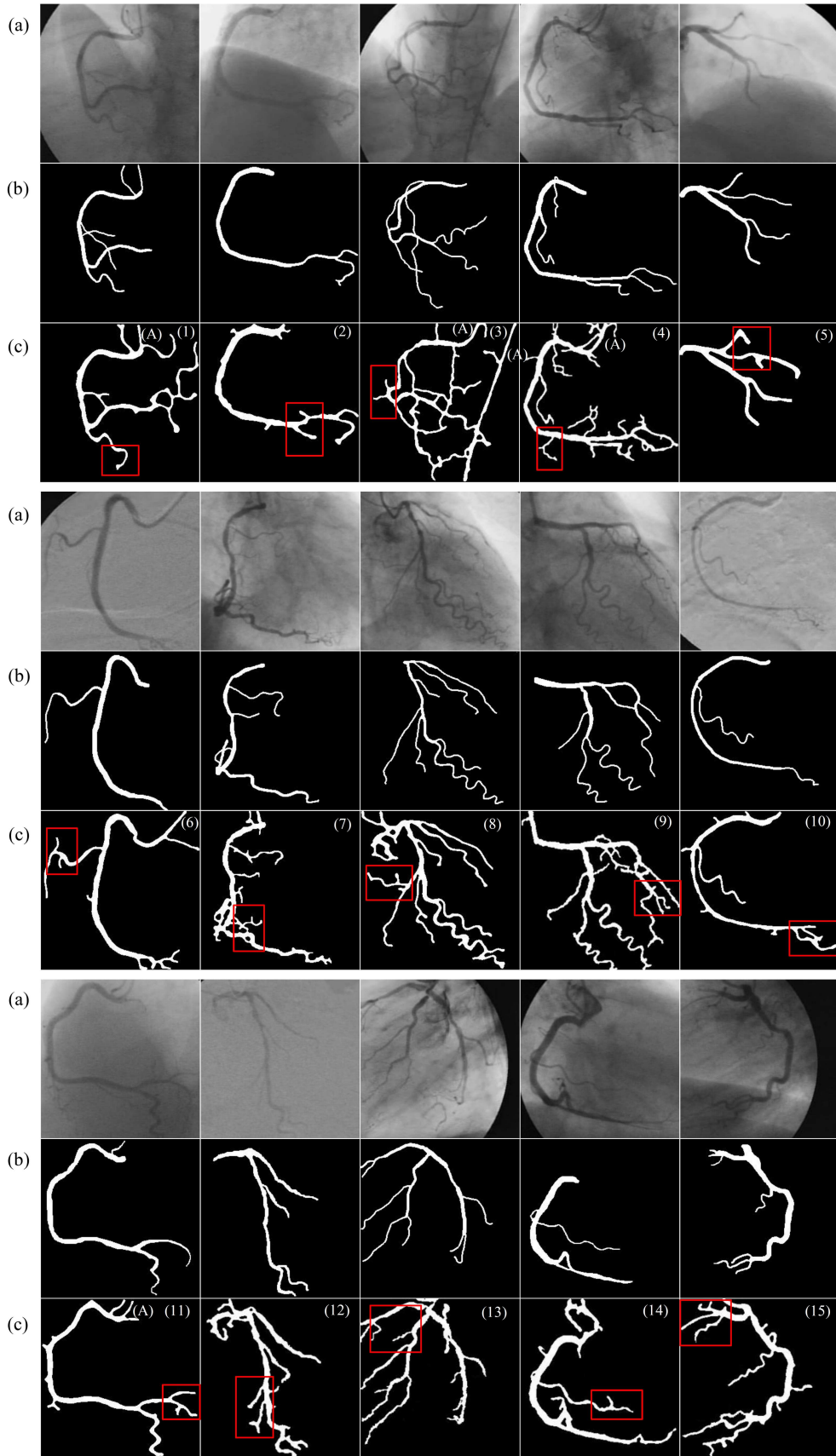
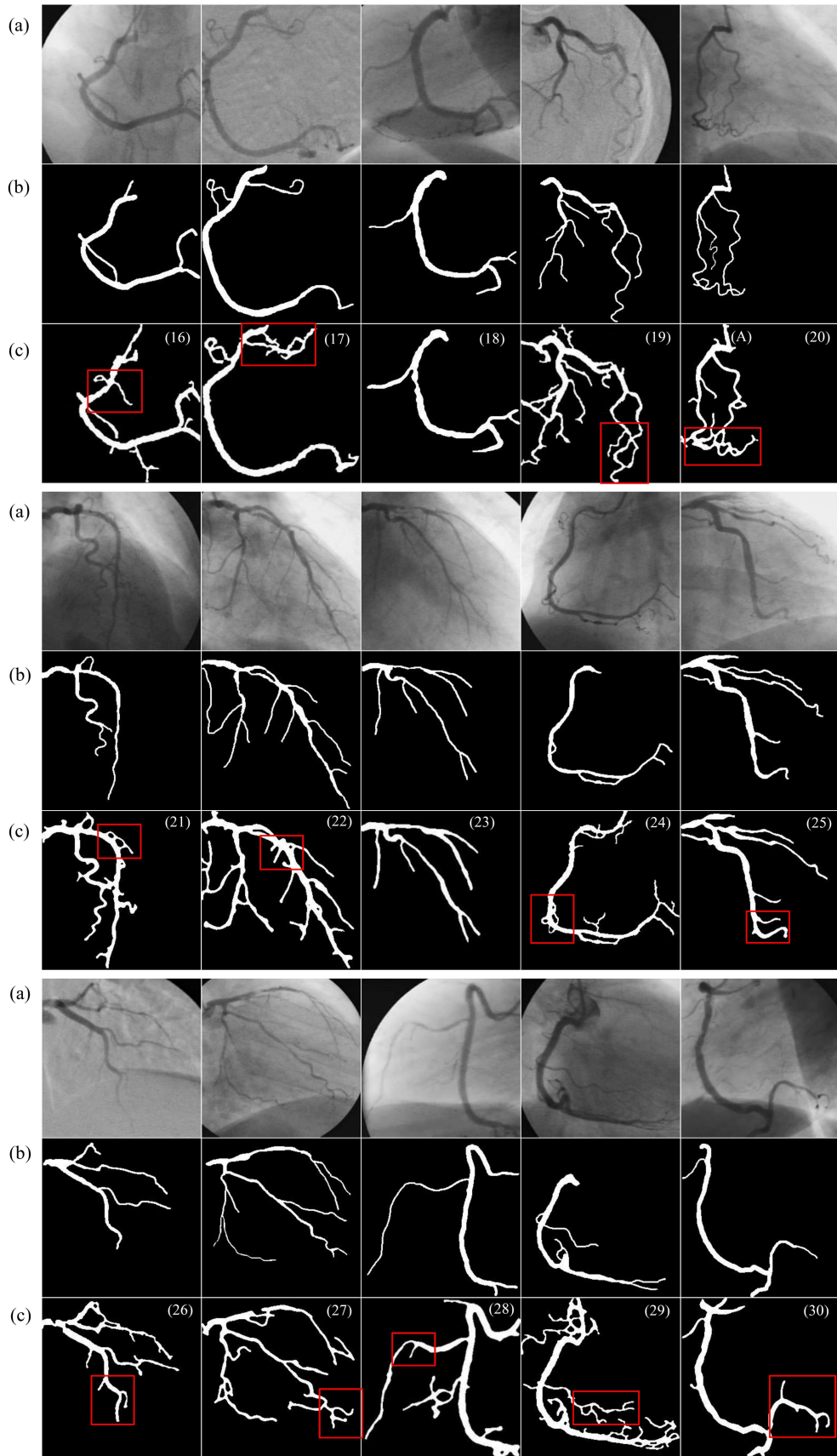Continued on the next page...

Fig. 5.   Results of coronary segmentation. Row (a) displays the original images. Row (b) shows cases of the ground truth (GT) images drawn by the vascular expert. Row (c) presents the segmented images acquired through the proposed method. Note: Fig. 5a and b comes from [11].

TABLE II

Potential parameters derived from the algorithm's output images.

HEART	TP	TN	FP	FN	n
HR001	3296	84556	1663	485	90000
HR004	3697	84463	1560	280	90000
HR010	3527	84363	1689	421	90000
HR011	2904	84110	2229	757	90000
HR016	4607	83400	1627	366	90000
HR023	2748	85187	1767	298	90000
HR024	4420	84117	892	571	90000
HR025	3729	84270	1556	445	90000
HR027	4100	83075	2436	389	90000
HR029	4536	82019	2986	459	90000
HR031	3092	85019	1513	376	90000
HR040	4886	83463	1093	558	90000
HR041	4027	83611	1900	462	90000
HR042	4071	83287	2292	350	90000
HR052	4211	84086	1586	117	90000
HR059	4543	83692	1313	452	90000
HR068	5028	82401	2252	319	90000
HR077	6685	80892	1809	614	90000
HR084	4446	83514	1485	555	90000
HR099	4377	82106	3159	358	90000
HR104	2697	85366	1561	376	90000
HR106	3579	84290	2061	70	90000
HR108	5641	80678	3027	654	90000
HR111	3420	85161	1182	237	90000
HR115	5224	82655	1275	846	90000
HR116	3528	84684	1419	369	90000
HR119	3968	83088	2066	878	90000
HR126	4964	81896	2941	199	90000
HR127	4228	83839	1483	450	90000
HR132	4268	83832	1585	315	90000
ALL	4148	83571	1847	434	90000

TABLE III

Performance measures for the overlapping portion of the vessel tree in the algorithm's output images and ground truth (GT) images.

HEART	SEN	SPE	ACC	AUC	DSC	t [s]
HR001	0.8717	0.9807	0.9761	0.9262	0.7542	1.4521
HR004	0.9296	0.9819	0.9796	0.9557	0.8007	1.3790
HR010	0.8934	0.9804	0.9766	0.9369	0.7698	1.5900
HR011	0.7932	0.9742	0.9668	0.8837	0.6605	1.3500
HR016	0.9264	0.9809	0.9779	0.9536	0.8222	1.5527
HR023	0.9022	0.9797	0.9771	0.9409	0.7269	1.4930
R024	0.8856	0.9895	0.9837	0.9376	0.8580	1.4370
HR025	0.8934	0.9819	0.9778	0.9376	0.7885	1.4510
HR027	0.9133	0.9715	0.9686	0.9424	0.7438	1.5216
HR029	0.9081	0.9649	0.9617	0.9365	0.7248	1.5821
HR031	0.8916	0.9825	0.9790	0.9370	0.7660	1.3230
HR040	0.8975	0.9871	0.9817	0.9423	0.8555	1.3254
HR041	0.8971	0.9778	0.9738	0.9374	0.7732	1.1840
HR042	0.9208	0.9732	0.9706	0.9470	0.7550	1.7826
HR052	0.9730	0.9815	0.9811	0.9772	0.8318	1.8525
HR059	0.9095	0.9846	0.9804	0.9470	0.8373	1.8068
HR068	0.9403	0.9734	0.9714	0.9569	0.7964	1.7759
HR077	0.9159	0.9781	0.9731	0.9470	0.8466	1.8558
HR084	0.8890	0.9825	0.9773	0.9358	0.8134	1.5299
HR099	0.9244	0.963	0.9609	0.9437	0.7134	1.7250
HR104	0.8776	0.9820	0.9785	0.9298	0.7358	1.5435
HR106	0.9808	0.9761	0.9763	0.9785	0.7706	1.5236
HR108	0.8961	0.9638	0.9591	0.9300	0.7540	1.4935
HR111	0.9352	0.9863	0.9842	0.9608	0.8282	1.6826
HR115	0.8606	0.9848	0.9764	0.9227	0.8313	1.5001
HR116	0.9053	0.9835	0.9801	0.9444	0.7978	1.5289
HR119	0.8188	0.9757	0.9673	0.8973	0.7294	1.5736
HR126	0.9615	0.9653	0.9651	0.9634	0.7597	1.6525
HR127	0.9038	0.9826	0.9785	0.9432	0.8139	1.8074
HR132	0.9313	0.9814	0.9789	0.9564	0.8179	1.5246
ALL	0.9049	0.9784	0.9747	0.9416	0.7826	1.5600

Imaging the coronary arteries of the heart involves capturing images from various angles using an X-ray machine. This results in different patterns of the blood vessels, and it is often challenging to distinguish one vessel from another within a given set of images. Since these images are two-dimensional, a specific angle may display a vessel's full width across the image, while many other vessels may overlap and appear rotated in the image's depth. As the blood vessels overlap, the pixel intensity increases, which results in the algorithm performing better in vein segmentation. The proposed method has the ability to focus on specific areas within the main image by adjusting parameters (K, R). These selected areas, treated as sub-images, are segmented separately, allowing for more accurate extraction of the tortuosity of the vessels (refer to Fig. 5c7–c9, c19, c20, c24). In some

images, external devices used in angiography, such as catheters and wires, are denoted by the letter "A" (see Fig. 5c1, c3, c4, c11, and c20).

Table II presents the calculated values of the mentioned potential parameters for 30 available images. The TN values, representing the highest numbers in the table, indicate the number of background pixels in each image. The second-highest values in the TP column correspond to the number of correctly identified vessel pixels. FP and FN denote the pixels that have been erroneously added or subtracted from the vessels, respectively. In the last column, the sum of all pixels ($n = 90000$) is provided, demonstrating the equality between the sum of the four mentioned parameters and confirming the accuracy of the algorithm's performance.

Table III presents performance measures for 30 images. The ACC and SPE values obtained for the 30 images are consistently close to each other, ranging from 96% to 98% and 97% to 99%, respectively. This demonstrates the algorithm's consistent

approach across different images. Notably, the Dice coefficient (DSC), which quantifies the similarity between the segmented vessel tree pattern and the ground truth pattern (GT), exhibits notable improvement compared to similar studies.

The last column in Table III displays the program execution time for each image. The average execution time is 1.56 s, which is shorter compared to the convolutional neural networks (CNN) (Lecun et al. [31]) method at 1.88 s and the multiscale analysis and artificial neural networks method at 1.89 s, respectively [11, 24]. These methods involve more extensive processing to achieve superior results, resulting in longer program execution times. In the proposed algorithm, the programs are executed using MATLAB software on a personal computer equipped with an Intel®Core™i7-5500U CPU @ 2.40 GHz.

4. Discussion

Given that the suggested algorithm yields a more comprehensive vascular network in comparison to similar research and ground truth (GT) images, the investigation of abnormalities within the blood vessels can offer valuable insights. To accomplish this, we have employed a second database that encompasses detailed information on typical angiography variations as references [10]. In light of this, we have chosen two images from the first database and four images from the second one, all showcasing various types of vascular abnormalities. These anomalies encompass blockages, vascular narrowing, blood clot formation, and fungal-related issues (Fig. 6).

In the primary images in Fig. 6, the lesion's position is indicated by red circles, while in the segmented images, it is marked with yellow circles. In the as and cs images, the bifurcation in the LCX is segmented. In the as image, which has lower contrast, the bifurcation appears as a constriction and slight depression in the vessels, whereas in the cs image, which has higher contrast, it appears as a clear severance or interruption of the vessels (Fig. 6).

In the segmented images bs and es, blockages and thrombosis were observed as sections where the vessels were severed or interrupted. Thrombosis, in particular, manifested in the ds image as a continuous constriction in a segment of the LCX vessel. When segmenting the RCA vessel with a mushroom-like ulcer, it appeared as a circular protrusion resembling a mushroom. The blood flow around this protrusion is restricted, and a narrow vein is visible (Fig. 6fs).

A visual comparison of the results of various methods displayed alongside each other can offer a clearer understanding of their differences. The outputs from 10 typical images processed by different methods are presented in columns next to one another (Fig. 7). To facilitate comparison, the output generated by the proposed algorithm is highlighted within a green box. The multiscale analysis and artificial neural networks method has improved true positives (TP) and demonstrated superior vessel segmentation performance compared to other methods by patching gaps and isolating the vessels. However, it still struggles detecting narrow veins. As a result, the sensitivity and accuracy criteria have not seen significant improvement compared to other methods [11]. The Gaussian matched filter (GMF)/entropy maximization method delivers strong overall segmentation results, but its performance can be compromised when dealing with holes, fractured vessels, and false positives along the image edges, leading to a reduction in its positive predictive value [32]. The U-Net method developed by Ronneberger et al. [33] exhibits the highest specificity and positive predictive value. Nevertheless, the segmentation outcome exhibits a notable number of false negative pixels in numerous images, leading to the presence of fractured vessels and a decrease in its overall effectiveness in extracting blood vessels [33]. The top-hat/background unification method and multiscale top-hat/background unification method attain a commendable classification accuracy, with their performance primarily hindered by the frequent occurrence of irregular boundaries and fractured vessels in the segmentation outcome. This leads to a decrease in their positive predictive value and Dice similarity coefficient compared to the ground truth [34, 35]. The segmentation performance of the multiline detector/threshold method (0.56) is influenced by the existence of irregular edges, gaps, and damaged blood vessels [36]. Nonetheless, their ability to segment is compromised by the presence of irregular edges, gaps, and damaged blood vessels. Among these, the Hessian-matrix-based/vessel repair method is the most adversely affected, leading to a reduction in its segmentation sensitivity [37]. In the method that relies on multiscale Gaussian templates, the accuracy and positive predictive value are influenced by the incorrect classification of pixels near the main coronary artery. This issue arises due to the robust detection responses produced by the multiscale Gaussian-matched filter for small tubular structures in the background [38]. The method that relies on single-scale Gabor filters often encounters an issue along the resulting image edges, which diminishes the method's sensitivity. The elevated occurrence of false positives in those regions is linked to the heightened detection intensities stemming from the utilization of solely the average vessel width as a single scale [39]. As depicted in Fig. 7 [11, 32–39], the proposed method, which utilizes KNN and MR, exhibits a more comprehensive depiction of the vascular network. Consequently, evaluation metrics such as accuracy, area under the curve (AUC), and Dice coefficient have shown substantial improvement. Moreover, the sensitivity and specificity parameters maintain their high values in comparison to other methods.
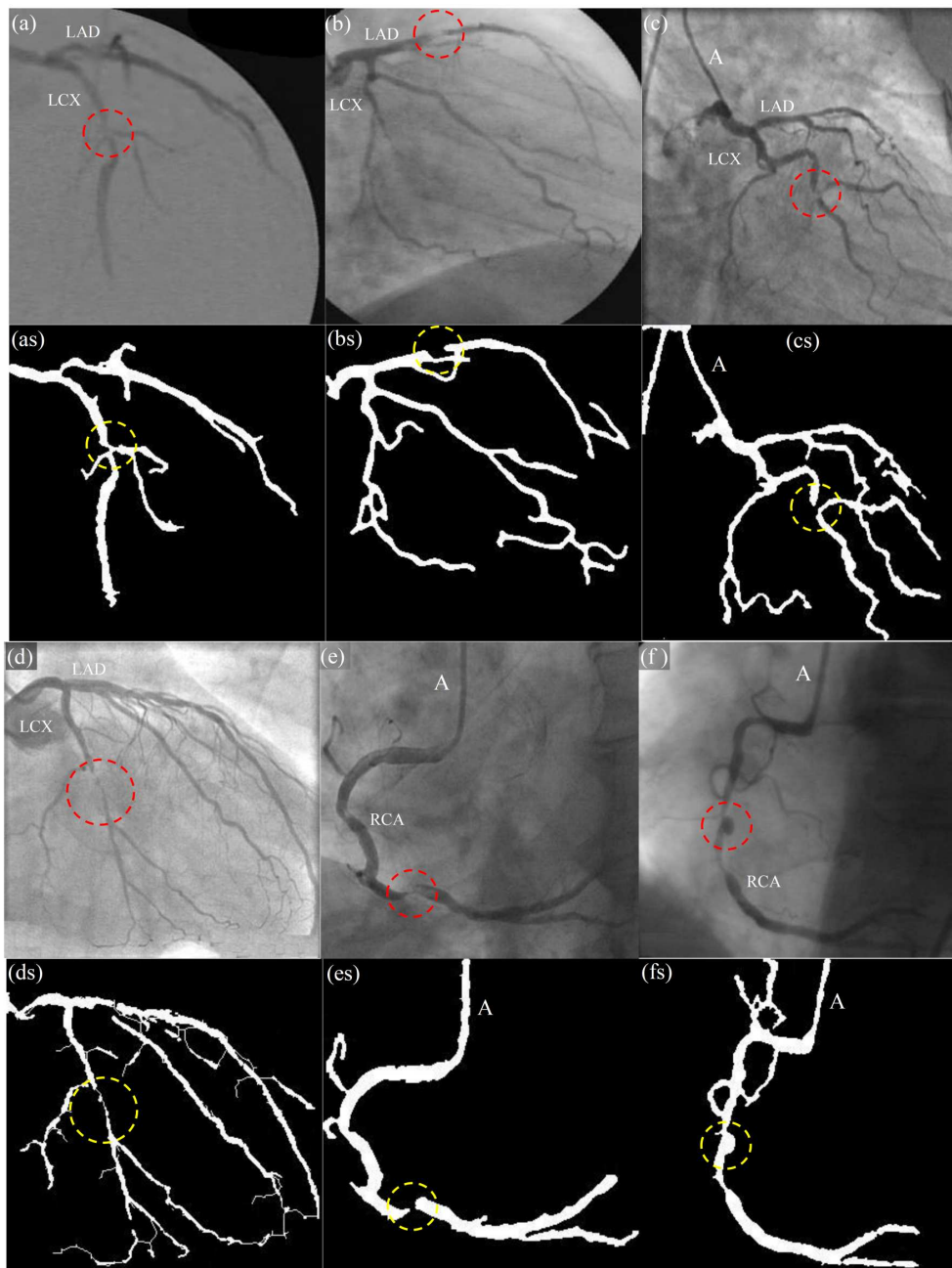
Fig. 6. Six sets of images depicting coronary vessels in the heart with associated lesions and their corresponding segmented images: (a, as) bifurcation in LCX; (b, bs) vessel occlusion in LAD; (c, cs) bifurcation in LCX; (d, ds) thrombus in LCX; (e, es) thrombus in RCA; (f, fs) mushroom-like ulcer in RCA.

While it is worth noting that the ground truth (GT) images crafted by cardiologists may not be entirely comprehensive, they remain the most reliable quantitative references for comparing numerical results. We evaluate various methods as described in Table IV [11, 32–39], and some of their segmented images are displayed in Fig. 7. For the multiscale analysis and artificial neural networks method [11], we achieved favorable evaluation values of ACC = 0.9698 and SPE = 0.9880, indicating strong results. However, the values for SEN, AUC, and DSC have comparatively lower results

when contrasted with other methods. Simultaneously, the U-Net (Ronneberger et al. [33]) method achieved the highest value of SEP = 0.9941 and a desirable value of ACC = 0.9645, whereas the remaining values are relatively low. The multiscale GMF/Otsu method [38] has achieved the highest value of SEN = 0.9326, but its other values have significantly decreased in comparison to other methods. While the other methods listed in Table IV have demonstrated favorable values for ACC and SPE, their values for SEN, AUC, and DSC are comparatively low [34–37, 39]. When comparing the
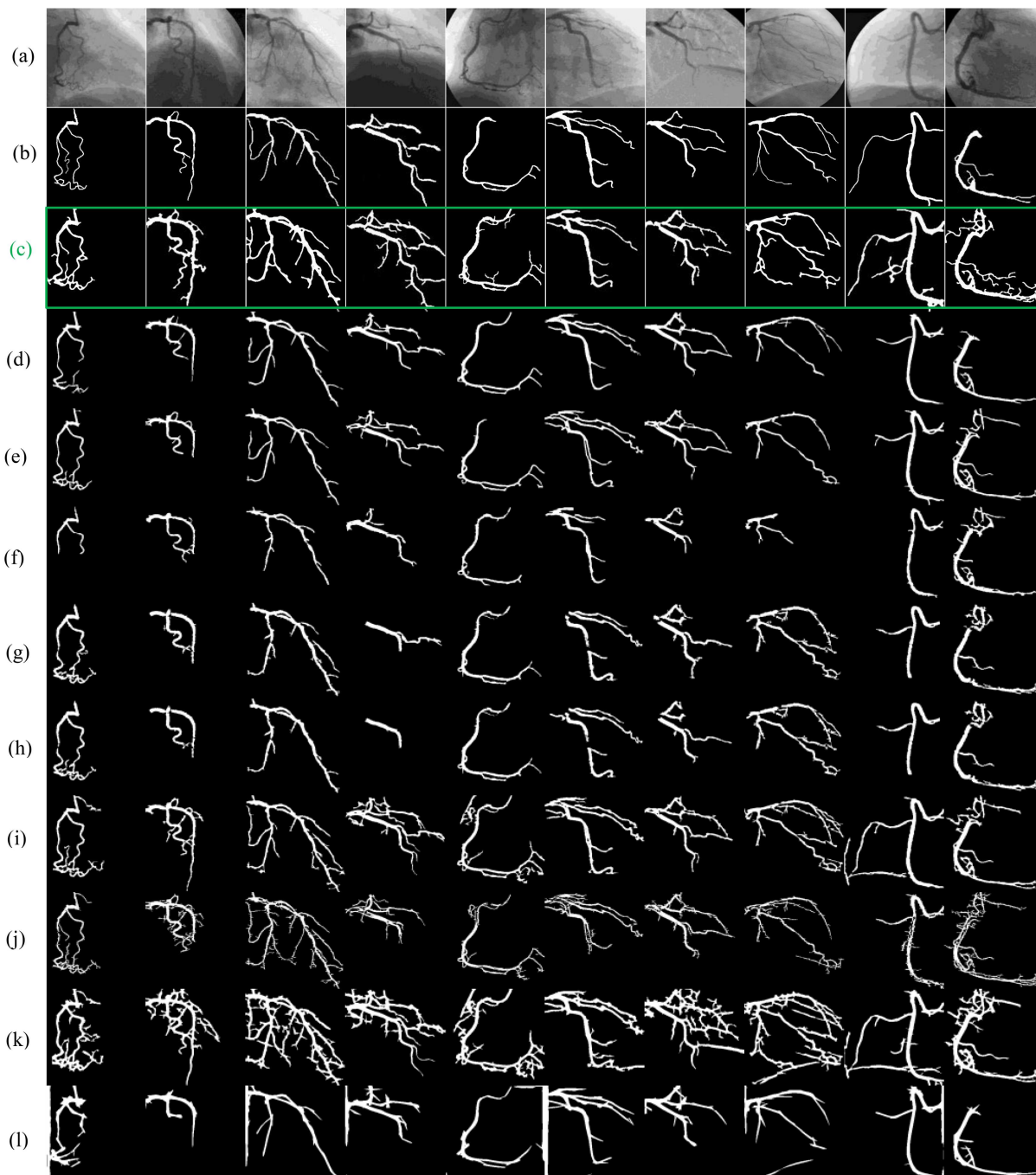
Fig. 7. Comparison of images that have been segmented using different methods: (a) original images; (b) ground truth images (GT); (c) images generated by the proposed method; (d) multiscale analysis and artificial neural networks method [11]; (e) GMF/entropy maximization method [32]; (f) U-Net method developed by Ronneberger et al. [33]; (g) top-hat/background unification method [34]; (h) multiscale top-hat/background unification method [35]; (i) multiline detector/threshold (0.56) method [36]; (j) Hessian-matrix-based/vessel repair method [37]; (k) multiscale Gaussian templates method [38]; (l) single-scale Gabor filters method [39].

evaluation results achieved by the proposed method to those of other methods, we observe substantial improvements in ACC = 0.9747, AUC = 0.9416, and DSC = 0.7826. Furthermore, the parameters SEN = 0.9049 and SPE = 0.9784 have remained consistently high.

In summary, the proposed method employs K parameters within the KNN clustering approach and divides images into sub-images with variable R, allowing for the dynamic generation of various segmentation images. Among these, those with higher evaluation metrics are chosen. This algorithm,

TABLE IV

Comparison of performance criteria between the proposed method and other methods

Authors	Segmentation method	SEN	SPE	ACC	AUC	DSC
F. Cervantes-Sanchez et al. [11]	multiscale analysis and artificial neural networks	0.6364	0.9880	0.9698	0.8122	0.6857
W. Kang, K. Wang et al. [32]	GMF/entropy maximization	0.6803	0.9825	0.9669	0.8314	0.6803
O. Ronneberger et al. [33]	U-Net	0.4216	**0.9941**	0.9645	0.7079	0.5515
S. Eiho, Y. Qian [34]	top-hat/background unification	0.6695	0.9757	0.9598	0.8226	0.6333
Y. Qian, S. Eiho et al. [35]	multiscale top-hat/background unification	0.6577	0.9766	0.9601	0.8172	0.6309
U.T. Nguyen et al. [36]	multiline detector/threshold (0.56)	0.8663	0.9606	0.9557	0.9135	0.6698
Y. Li. et al. [37]	Hessian-matrix-based/vessel repair	0.6484	0.9712	0.9545	0.8098	0.5962
I. Cruz-Aceves et al. [38]	multiscale GMF/Otsu	**0.9326**	0.9250	0.9326	0.9288	0.5644
F. Cervantes-Sanchez et al. [39]	single-scale Gabor filters/Otsu	0.3920	0.9661	0.9196	0.6791	0.3898
Proposed method	KNN+MR	**0.9028**	0.9780	**0.9743**	**0.9404**	**0.7783**

capable of segmenting thinner blood vessels, has been employed for coronary vessel lesion detection and has successfully depicted these lesions in the final images. The algorithm conducts segmentation both horizontally and vertically in one dimension, offering the potential for further enhancement through segmentation at different angles, which could enhance its accuracy and be a topic for future research. Based on the results presented in the tables and figures of this study, it can be argued that the proposed method has the potential for use as a computer-aided diagnosis tool.

5. Conclusions

This article focuses on using the KNN (*K*-nearest neighbors) clustering method to segment coronary vessel images obtained through X-ray angiography. Since the brightness intensity of vein pixels in these images is relatively low, a top-hat conversion technique is employed to enhance the brightness of the image. The segmentation process involves two distinct pathways for thick vessels and narrow vessels. This separation allows for effective removal of background noise through operations such as morphological reconstruction, vessel skeletonization, and pruning. Finally, thin vessels are connected to the thick vessels to complete the vessel tree. In this particular stage, a convolution filter is defined to eliminate any remaining noise in the image.

The evaluation of the achieved results with ground truth (GT) images demonstrates the success of the proposed method, with the performance criteria attaining high and satisfactory values. Notably, the three specific values of these criteria are ACC (accuracy) = 0.9747, SPE (specificity) = 0.9784, and SEN (sensitivity) = 0.9049. The proposed algorithm is employed to identify patterns of lesions within the blood vessels, and it effectively segments

the visual representation of these diseases. The algorithm exhibits the capability to detect thin vessels characterized by low light intensity. Hence, this algorithm holds potential for application in handling other intricate patterns, such as vessel segmentation.

The dataset used in this research comprises 130 X-ray angiographic images, which are freely available for use by the scientific community. The images can be accessed and downloaded from the website (http://personal.cimat.mx:8181/_ivan.cruz/DB_Angiograms.html) [11].

References

[1] K. Iyer, C.P. Najarian, A.A. Fattah et. al., *Sci. Rep.* **11**, 18066 (2021).

[2] K. Pang, D. Ai, H. Fang, J. Fan, H. Song, J. Yang, *Comput. Med. Imaging Graph.* **89**, 101900 (2021).

[3] Z. Huang, Q. Li, T. Zhang, N. Sang, H. Hong, *IET Image Process.* **12**, 254 (2018).

[4] J. Jun, F. Li, L. Changling, X. Yongqing, H. Jingsong, L. Xiaochang, D. Liang, H. Xinyang, W. Jianan, X. Jianping, *Quant. Imaging. Med. Surg.* **11**, 4543 (2021).

[5] C. Kirbas, F. Quek, *ACM Comput. Surv.* **36**, 81 (2004).

[6] D. Lesage, E. D. Angelini, I. Bloch, G.A. Lea, *Med. Image Anal.* **13**, 819 (2009).

[7] G. Läthén, Ph.D. thesis, 2010.

[8] K. Drechsler, Ph.D. thesis, 2012.

[9] K. Mardani, K. Maghooli, *Biomed. Signal Process. Control* **69**, 102837 (2021).

[10] C.M. Gibson, *Coronary Angiography*, www.wikidoc.org.

[11] F. Cervantes-Sanchez, I. Cruz-Aceves, A. Hernandez-Aguirre, M.A. Hernandez-Gonzalez, S.E. Solorio-Meza, *Appl. Sci.* **9**, 5507 (2019).

[12] N.A. Otsu, *IEEE Trans. Syst. Man Cybern.* **9**, 62 (1979).

[13] T. Ridler, S. Calvard, *IEEE Trans. Syst. Man Cybern.* **8**, 630 (1978).

[14] W. Niblack, *An Introduction to Digital Image Processing*, Strandberg Publishing Company, Birkeroed (Denmark) 1985.

[15] W.H. Tsai, *Comput. Vision Graph. Image Process.* **29**, 377 (1985).

[16] J. Kittler, J. Illingworth, J. Föglein, *Comput. Vision Graph. Image Process.* **30**, 125 (1985).

[17] J. Sauvola, M. Pietikäinen, *Pattern Recognit.* **33**, 225 (2000).

[18] J. Kapur, P. Sahoo, A. Wong, *Comput. Vision Graph. Image Process.* **29**, 273 (1985).

[19] R.C. Gonzalez, R.E. Woods, *Digital Image Processing*, Pearson, New York 2018.

[20] S. Uddin, I. Haque, H. Lu, M.A. Moni, E. Gide, *Sci. Rep.* **12**, 6256 (2022).

[21] J. Xia, J. Zhang, Y. Wang, L. Han, H. Yan, *Pattern Recognit.* **121**, 108177 (2022).

[22] A.J. Gallego, J.R. Rico-Juan, J.J. Valero-Mas, *Pattern Recognit.* **122**, 108356 (2022).

[23] D. Sisodia, D. Sisodia, *Eng. Sci. Technol. Int. J.* **28**, 101011 (2022).

[24] W. Kang, Y. Li, Q. Wang, in: *Proc. of the 2013 2nd Int. Conf. on Measurement, Information and Control, Harbin (China)*, Vol. 1, 2013, p. 696.

[25] J.M. White, G.D. Rohrer, *IBM J. Res. Dev.* **27**, 400 (1983).

[26] A. Rosenfeld, P.D.L. Torre, *IEEE Trans. Syst. Man, Cybern.* **13**, 231 (1983).

[27] N.R. Pal, S.K. Pal, *Signal Process.* **16**, 97 (1989).

[28] Z. Cömert, A.F. Kocamaz, *Acta Phys. Pol. A* **132**, 3 (2017).

[29] G. Demenko, M. Szymanski, R. Cecko, E. Kuśmierek, M. Lange, K. Wegner, K. Klessa, M. Owsianny, *Acta Phys. Pol. A* **121**, A-86 (2012).

[30] Y. Wang, X. Gao, Y. Wang, J. Sun, *Optik* **241**, 167175 (2021).

[31] Y. Lecun, L. Bottou, Y. Bengio, P. Haffner, *Proc. IEEE* **86**, 2278 (1998).

[32] W. Kang, K. Wang, W. Chen, W. Kang, in: *Proc. of the 2009 2nd Int. Congress on Image and Signal Processing, Tianjin (China)*, 2009.

[33] O. Ronneberger, P. Fischer, T. Brox, in: *Int. Conf. on Medical Image Computing and Computer-Assisted Intervention*, Springer Nature, Cham (Switzerland) 2015, p. 234.

[34] S. Eiho, Y. Qian, in: *Proc. of the Computers in Cardiology*, 1997, p. 525.

[35] Y. Qian, S. Eiho, N. Sugimoto, M. Fujita, in: *Proc. of the Computers in Cardiology*, vol. 25, 1998, p. 765.

[36] U.T. Nguyen, A. Bhuiyan, L.A. Park, K. Ramamohanarao, *Pattern Recognit.* **46**, 703 (2013).

[37] Y. Li, S. Zhou, J. Wu, X. Ma, K. Peng, in: *Proc. of the 2012 4th Int. Conf. on Computational and Information Sciences, Chongqing (China)*, 2012, p. 468.

[38] I.C. Aceves, F.S. Cervantes, M.S.A. Avila-Garcia, *J. Healthc. Eng.* **2018**, 5812059 (2018).

[39] F.C. Sanchez, I. Cruz-Aceves, A.H. Aguirre et. al., *Comput. Intell. Neurosci* **2016**, 2420962 (2016).